# EXPERIMENTAL STUDY OF LASER-DRIVEN COMPRESSION OF SPHERICAL GLASS SHELLS

G. CHARATIS, J. DOWNWARD, R. GOFORTH, B. GUSCOTT, T. HENDERSON, S. HILDUM, R. JOHNSON, K. MONCUR, T. LEONARD, F. MAYER, S. SECALL, L. SIEBERT, D. SOLOMON, C. THOMAS
KMS Fusion, Inc., Ann Arbor, Mich.,
United States of America

Abstract

EXPERIMENTAL STUDY OF LASER-DRIVEN COMPRESSION OF SPHERICAL GLASS SHELLS.

Laser-driven compression, core heating, and neutron generation are experimentally observed when DT-filled glass shells are illuminated by intense laser radiation. Requirements for obtaining strong compressions and neutron generation include nearly uniform illumination, energies on-target greater than 0.7 J per nanogram of shell mass, symmetric target disassembly and on-target intensities of $10^{15}$ W/cm$^2$. The laser system, target illumination optics, targets, and laser target diagnostics are described in detail.

## 1. INTRODUCTION

The experiments at KMS Fusion are designed to test the theoretical concepts of laser-driven fusion [1,2]. These theoretical concepts indicate that spherically symmetric target heating by intense laser irradiation can produce ablation-driven compression and heating of the target core to thermonuclear conditions. A number of investigators have reported neutron generation from $CD_2$ and LiD spheres [3, 4] and solid deuterium targets [5, 6]. The KMS Fusion experiments have provided the first direct observation of target compression and core heating resulting in neutron generation. The neutron generation from deuterium-tritium pressurized spherical glass shells is experimentally correlated with target compression inferred from X-ray pinhole photographs. The coupling of laser energy into target compression is studied by X-ray and particle kinetic-energy measurements, and the partition of on-target laser energy into radiation and plasma kinetic energy is experimentally determined.

## 2. THE KMSF LASER SYSTEM

The KMSF laser system consists of a mode-locked YAG oscillator, a CILAS VK640 laser, an additional 80-mm rod amplifier, and seven 10-cm-clear-aperture GE disk amplifier units. A single 30-ps pulse is selected from the oscillator by a laser-triggered spark gap and double Pockels cell combination. It is then divided into a pre-determined number of temporally delayed pulses, which are suitably attenuated and spatially recombined into a tailored pulse shape. The full width half maximum (FWHM) of the stacked pulse used in the laser target experiments has ranged from 0.03 to 1.0 ns with on-target laser energies up to 230 J.

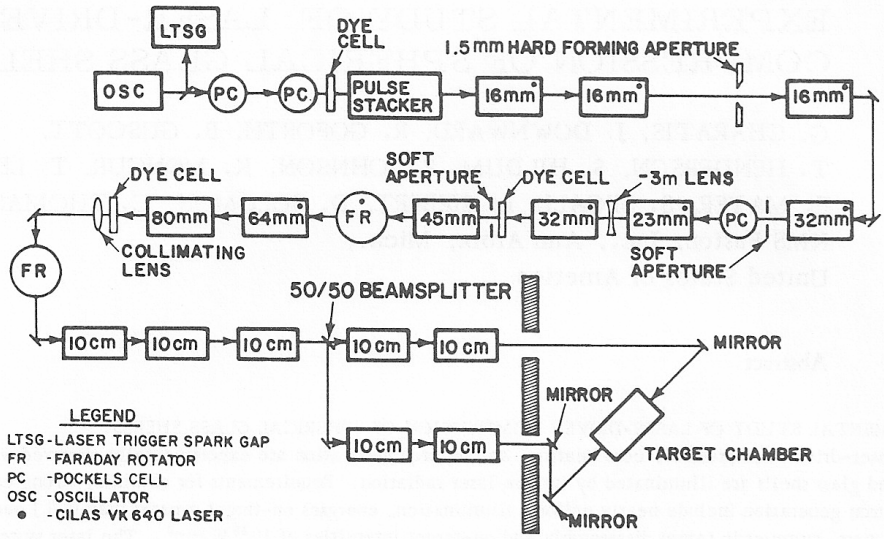


FIG.1. The KMSF laser system.

The tailored pulse is amplified by the VK640 laser and the 80-mm amplifier and then travels 30 m before entering the GE disk amplifiers (Fig.1). The pulse emerges from the amplifier train horizontally polarized. Successful operation of the KMSF laser system requires

a) Apodized apertures to minimize the formation of diffraction rings in the beam.
b) Isolating Pockels cells to prevent self-oscillation and aid in target isolation (contrast ratio > $10^4$).
c) Faraday rotators to protect the laser from target-reflected energy.
d) Saturable dye cells for target isolation from laser fluorescence (amplified spontaneous emission).

Fluorescence energy incident on the target is monitored with an integrating photodiode. Normally, targets are exposed to 0.2 - 5 mJ of fluorescence preceding the main pulse. Fluorescence levels above 5 mJ can influence the target response.

## 3. TARGET ILLUMINATION AND ALIGNMENT

The target illumination system delivers nearly uniform laser energy to the targets, at essentially orthogonal incidence over the spherical surface, using two aspheric f/0.6 lenses and two ellipsoidal mirrors [7]. The target is placed at the common focus of the two mirrors (Fig.2). The mirrors effectively increase the 80° cone angle of each f/0.6 lens to a 144° cone angle at the target. Small longitudinal displacements of the lenses and mirrors away from their coincident-focus position are used to introduce intentional aberrations which make the target illumination nearly uniform over the complete target surface.

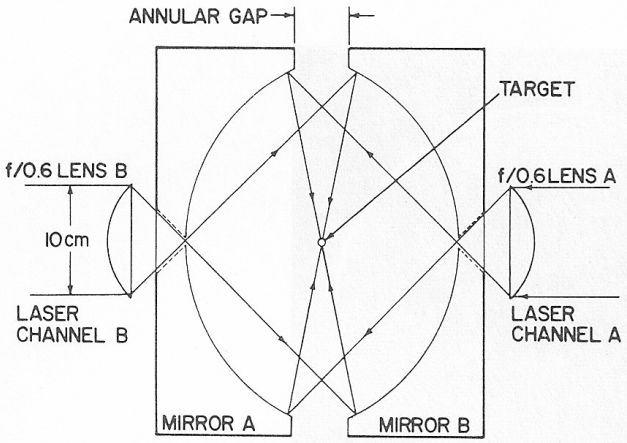


FIG.2. The KMSF two-beam ellipsoidal mirror target illumination system.

The target is aligned with a continuous-wave YAG laser which is collinear with and is divergence-metched to the main laser. A television camera views the YAG light reflected from the target via a 1% beamsplitter in each channel. A second television camera monitors the target focal position along the optic axis.

## 4. THE TARGETS

The targets used in this series of experiments are spherical glass shells filled with deuterium or deuterium-tritium (DT) gas mixtures and mounted on 3-$\mu$m alumina fibers.

Optimization of laser-target experimental parameters requires that there be available targets possessing an extensive range of diameters, wall thicknesses, and partial pressures of the fuel gases. The outside diameters vary from 30 to 700 $\mu$m; the wall thicknesses vary from 0.5 to 12 $\mu$m with an observed minimum variation of the wall thickness of any single target of 5%. The total fuel gas pressures vary from 1 to 100 atmospheres.

Shells to be used as targets are characterized individually. The characterization consists of:

a) A determination of the mean wall thickness and wall non-uniformity by a computer analysis of the optical density measured on a contact microradiograph of the shell (Fig.3a).
b) A scanning electron micrograph of the target surface (Fig.3b).
c) Measurement of the shell's outer diameter and circularity using an image-splitting eyepiece and gauging unit (Fig.3c).

The shells are filled to the desired pressures by permeation of the gases through the shell walls. To accomplish this, the shells are inserted into an autoclave which is then pressurized at room temperature with gas or a mixture of gases to pressures equal to the desired fill pressures. Filling is

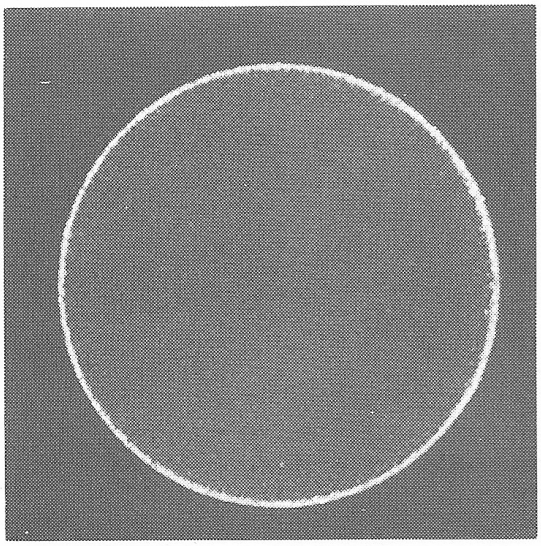

(a)

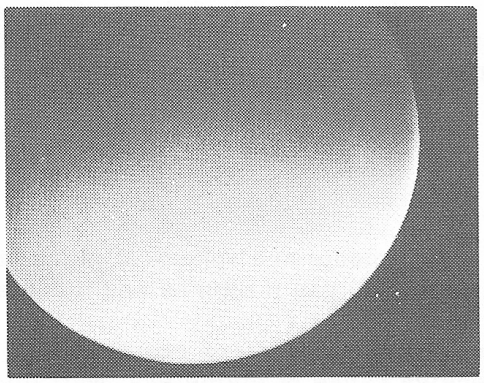

(b)

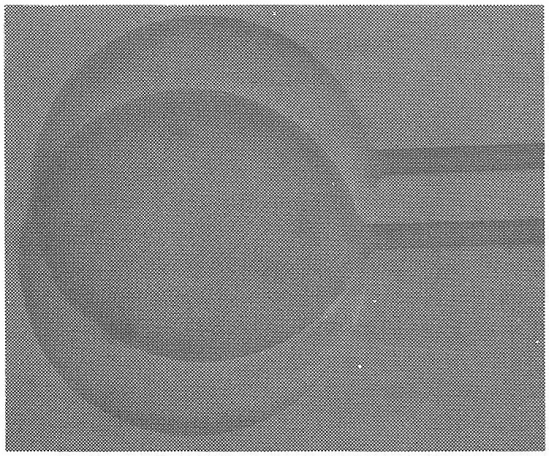

(c)

FIG. 3. Stages of target characterization:
a) radiographic negative;
b) scanning electron micrograph;
c) image-splitting eyepiece.

achieved by maintaining the autoclave at an elevated temperature long enough to assure that the internal pressures of all the shells are within a predesignated fraction of the autoclave pressure. Upon completion of the filling process, the shells are removed from the autoclave and stored at room temperature.

The pressure and composition of the gas in a batch of shells are obtained by rupturing a statistical sample of the shells, and measuring or analysing individually the gas released by each ruptured shell. Total gas pressure is measured by rupturing a shell in glycerol, thereby forming a bubble whose diameter can be related to the initial gas pressure. The toral quantity of tritium is determined by rupturing a shell inside an ionization chamber and measuring the total radioactivity. Gas ratios are measured by rupturing a shell in the ionizer of a quadrupole mass spectrometer.

The quantity of gas in an individual shell is measured non-destructively by freezing the fill gas with a cryogenic apparatus, and then optically measuring the dimensions of the frozen DT within the shell. This optical-cryogenic technique is useful for determining whether fuel gas remains inside a shell that has been exposed to fluorescence (or other prepulse energy) but not to the main laser pulse.

## 5. LASER TARGET DIAGNOSTICS

The 50-mm annular gap between the ellipsoidal mirrors provides a direct-view diagnostic region (DVDR). Plasma, optical, and X-ray diagnostics are arranged circumferentially in this region as shown in Figure 4. The annular gap at the periphery of the mirror subtends a solid angle of $0.53\pi$ steradians at the target. Target diagnostics not located in the DVDR are the neutron-detection diagnostics (Fig.5) and the target-reflectivity diagnostics (Fig.6).

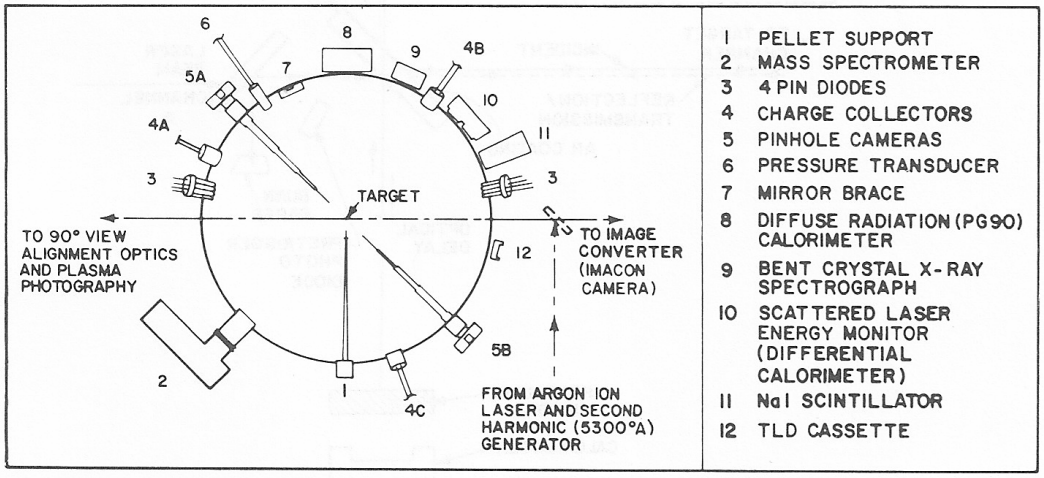


FIG.4. Diagnostics located in the DVDR.

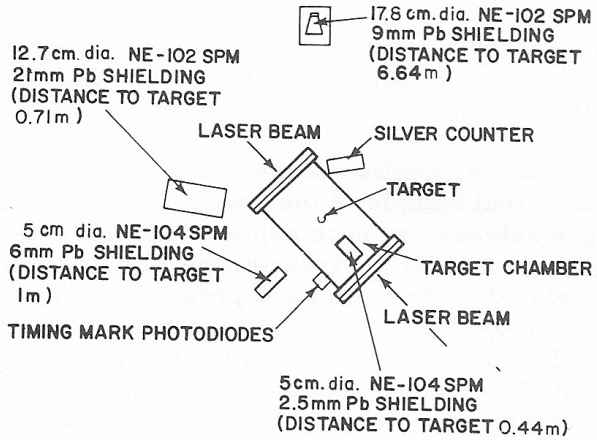


FIG. 5. Location of neutron detectors.

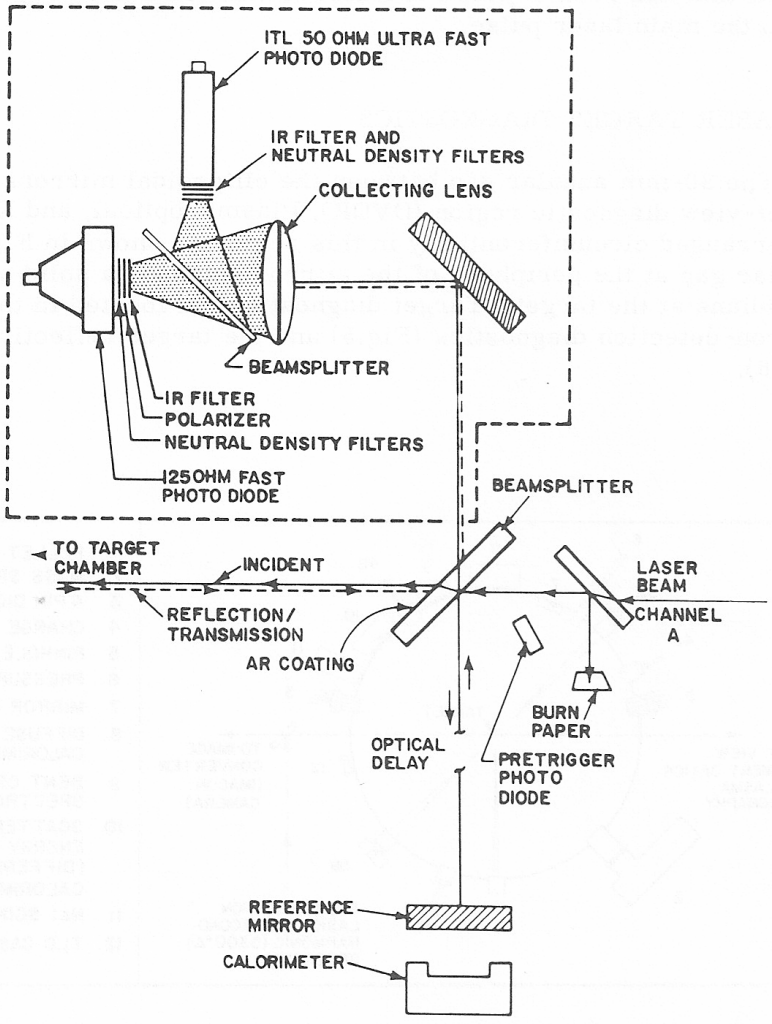


FIG. 6. Pulse shape, laser energy, and target reflectivity diagnostics.

## 5.1. Optical energy measurements

The laser radiation is measured by fast photodiodes and calorimeters in both laser channels to determine the laser pulse shape, the energy on the target, the energy reflected and transmitted back through the mirror illumination system, and the energy refracted and scattered at 90° to the optic axis that escapes through the DVDR (Fig.4). One percent of the incoming horizontally polarized radiation is split off with a beamsplitter (Fig.6) and transmitted to a reference mirror. Part of the radiation passes through this mirror into a calorimeter. The energy measured by the calorimeter, corrected for the transmission losses through the optical system, provides a direct measure of the on-target energy. The light reflected from the reference mirror is returned to the fast photodiodes 6 ns before the reflected light from the target. One fast photodiode covered with an infra-red polarizer detects horizontally polarized light. The other ultra-fast photodiode (without a polarizer) detects the sum of the horizontally and vertically polarized back-reflected radiation. These photodiodes measure the total fraction of the incident energy returned through the mirror system. The laser pulse width (FWHM) is obtained using the ultrafast ($\leq$ 0.1 ns rise-time), 50-Ohm ITL photodiode[1] coupled directly to the deflection plates of a Tektronix 7904 oscilloscope ($\leq$ 0.2 ns rise-time). The photodiodes and oscilloscope have a combined measured rise-time of 0.22 nsec with less than 10% aberration. Improved time resolution ($\sim$ 10 ps) is obtained using an Imacon 600 image converter-intensifier streak camera.

## 5.2. X-ray energy and spectral measurement

Total emitted X-ray energy, both line and continuum, is measured by $CaF_2$(Dy) thermoluminescent dosimeters (TLD) [9]. The spectral distribution of the continuum radiation above 3 keV is determined by the X-ray filtration technique [10] using thin foil attenuators covering the TLDs and silicon PIN X-ray diodes. Detector readings are then compared with temperature-parameterized theoretical curves.

TLD detectors covered by thin K-edge foils of 25 $\mu$m or less observe the lower energy portion of the spectrum, and silicon X-ray diodes covered by thicker foils or foils of higher atomic number sample the harder portion of the X-ray spectrum. Figures 7a and 7b show typical TLD and diode data. The TLD data in Fig. 7a are best fitted by a 1.2 keV temperature; the diode readings are best fitted by a 10 keV temperature. Total X-ray energy as measured by unshielded TLD detectors increases approximately as the 1.5 power of the laser energy on target for typical targets such as those shown in Table I.

Preliminary results from measurements of the X-ray line radiation using a bent crystal spectrograph (Fig.4) indicate strong line emission from one and two electron silicon ions. Estimates of electron temperature and density are made using line ratios of allowed and forbidden lines [11].

---

[1] Instrument Technology Ltd., UK.

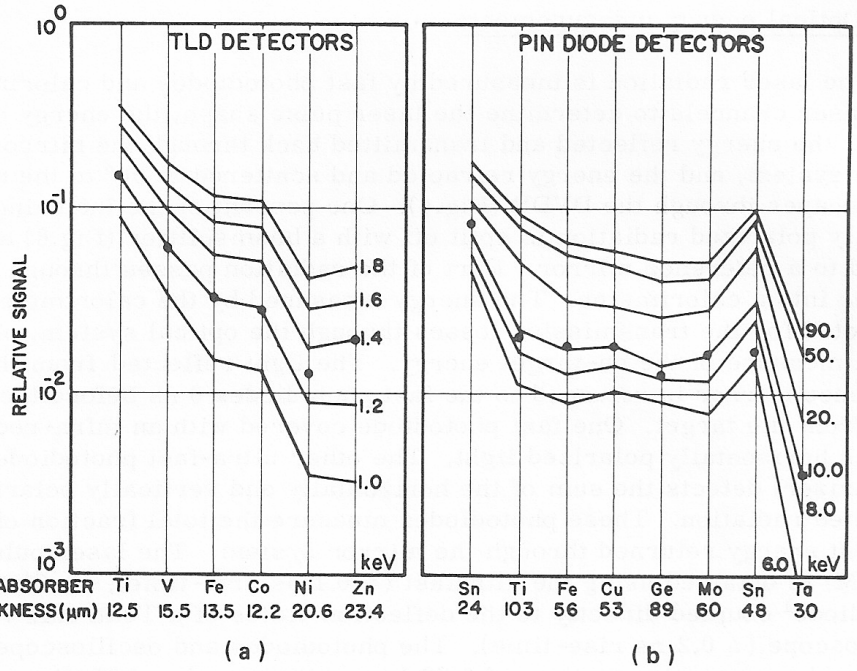


FIG. 7. a) Typical fit of theoretical temperature-parameter curves to TLD data.
b) Fit of theoretical curves to silicon X-ray diode data.

## 5.3. Plasma measurements

Measurements of the target mass ablation and total ion kinetic energy are made with several charge collectors located at different azimuthal positions in the DVDR (Fig.4). The charge collectors are biased to collect ion current. Charge-collector oscilloscope traces (Fig.8) are compared to determine the degree of symmetry of the target disassembly. The initial sharp spike is produced by photoelectron emission from the collector surface and is coincident with the laser-energy deposition. The first small ion peak following the photoelectron spike is produced by "fast" ions whereas the large ion peak is produced by "slow" ions. The $4\pi$ rate of mass collection is determined from

$$\dot{m} = \frac{\Omega}{\Delta\Omega} \frac{V(t)\, A\, m_p}{R_L\, e\, Z_{eff}}$$

where $\Omega/\Delta\Omega$ is the inverse of the collector fractional solid angle, V(t) is the oscilloscope voltage, $R_L$ is the load resistor (50 Ohm), A is the atomic weight, $m_p$ is the proton mass, e is the electron charge, and $Z_{eff}$ is the effective charge number of the collected ions. The effective charge includes a correction for secondary electron emission from the collector surface[2], and is

[2] The secondary emission correction is taken from the work of LARGE, L.N. – see KREBS, K.H., Fortschr. Phys. 16 (1968) 452. It is assumed that the ionized $SiO_2$ impacting on the copper of the charge collectors has a secondary emission coefficient close to $Ne^+$ impacting on tungsten.

TABLE I. CHARACTERISTICS OF NEUTRON EVENTS

| NEUTRON EVENT | 1 | 2 | 3 | 4 | 5 |
|---|---|---|---|---|---|
| Target Diameter ($\mu$m) | 66 | 64 | 78 | 64 | 71 |
| Wall Thickness ($\mu$m) | 0.9 | 0.8 | 0.6 | 0.9 | 0.8 |
| Target Deuterium-Tritium Pressure (atm) | 18-13 | 18-13 | 18-13 | 18-13 | 18-13 |
| $E_T$ - Energy on Target (J) | 40.9 | 48.3 | 55.7 | 52.0 | 61.2 |
| $M_I$ - Target Mass (ng) | 27 | 23 | 25 | 28 | 28 |
| $E_T/M_I$ (J/ng) | 1.51 | 2.14 | 2.21 | 1.86 | 2.19 |
| I - Average Intensity ($W/cm^2 \times 10^{15}$) | 1.35 | 1.81 | 1.24 | 1.78 | 1.64 |
| Laser Pulsewidth (nsec) | 0.32 | 0.30 | 0.34 | 0.30 | 0.34 |
| Neutron Yield ($\times 10^5$) | 4 | 3 | 3 | 2.5 | 2.5 |
| Reflected Laser Energy (J) | 17.7 | 22.1 | 25.3 | 23.6 | 28.6 |
| Depolarized Laser Energy (J) | 4.5 | 4.1 | 4.7 | 4.3 | 4.8 |
| Scattered Laser Energy Into DVDR (J) | 2.9 | 4.6 | 4.4 | 5.4 | 3.5 |
| Target Absorbed Energy (J) | 8.0 | 11.4 | 14.4 | 14.0 | 8.2 |
| Target X-ray Energy (J) | 0.8 | 0.8 | --- | 0.9 | 0.6 |
| Charge Collector Symmetry (Ion Mass Collected by 4A/ Ion Mass Collected by 4B) | 0.94 | 0.87 | 0.93 | 0.93 | 1.00 |
| Laser Fluorescence on Target (mJ) | 2.2 | 5.0 | 2.5 | 3.5 | 2.2 |

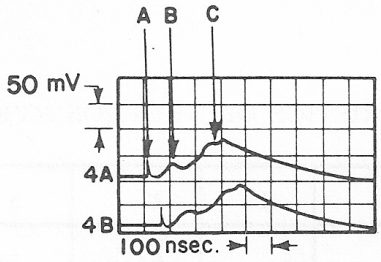


FIG. 8. Typical charge collector oscilloscope traces: A — photoelectron emission, B — "fast" ions, C — "slow" ions.

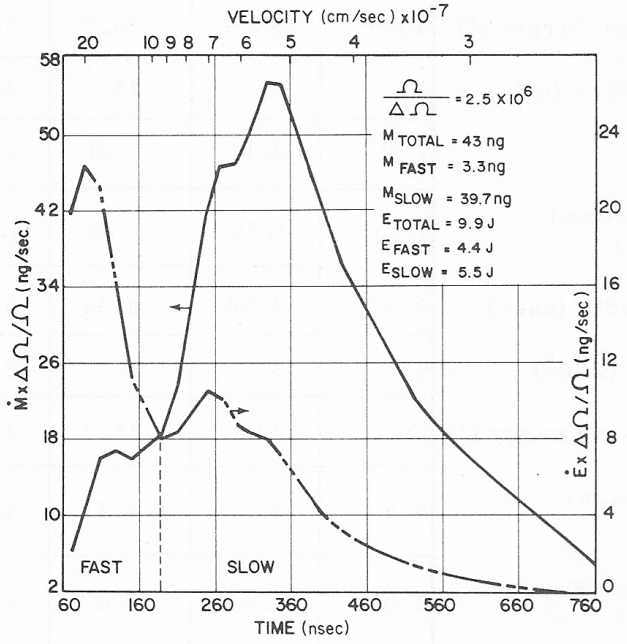


FIG. 9. Mass and energy collection rate.

given by $Z_{eff} = \bar{Z} + 4.65 \times 10^{-8}$ v, where $\bar{Z}$ is the average ion charge number and v is the ion velocity (cm/s). An estimate of $\bar{Z}$ is obtained from the mass spectrometer measurements. If the target glass shells are completely ionized, the collected ions will have an average charge state of $Z = 10$.

In a similar manner, the $4\pi$ rate of kinetic energy collection is calculated from $\dot{E}_{ke} = \frac{1}{2}\dot{m}v^2$. Here, $v = R/t$, where R is the target-to-detector distance and t is time measured from laser deposition. Figure 9 shows $\dot{m}(t)$ and $\dot{E}_{ke}(t)$ curves determined from the lower trace of Fig. 8. Notice that the "fast" ions, although they amount to only ~ 8% of the ablated mass, carry ~ 45% of the target kinetic energy. The total mass and kinetic energy are determined from numerical integration of the $\dot{m}$ and $\dot{E}_{ke}$ curves.

TABLE I-A

| Neutron Event | 1 | 2 | 3 | 4 | 5 |
|---|---|---|---|---|---|
| Target Diameter ($\mu$m) | 42 | 50 | 40 | 43 | 59 |
| Wall Thickness ($\mu$m) | 0.5 | 0.6 | 0.5 | 0.4 | 0.9 |
| Target Deuterium-Tritium Pressure (atm) | 18-13 | 18-13 | 18-13 | 18-13 | 18-13 |
| $E_T$ - Energy on Target (J) | 58.8 | 67.6 | 62.8 | 69.6 | 44.7 |
| $M_I$ - Target Mass (ng) | 7 | 12 | 6 | 6 | 25 |
| $E_T/M_I$ (J/ng) | 8.5 | 5.7 | 10.0 | 12.0 | 1.8 |
| I - Average Intensity ($W/cm^2 \times 10^{15}$) | N.M. | 3.6 | 6.0 | 5.7 | 2.4 |
| Laser Pulsewidth (nsec) | N.M. | 0.30 | 0.30 | 0.35 | 0.25 |
| Neutron Yield ($\times 10^6$) | 7.0 | 5.2 | 5.2 | 4.5 | 4.0 |
| Reflected Laser Energy (J) | N.M. | 27.6 | 25.2 | 29.7 | 18.1 |
| Depolarized Laser Energy (J) | N.M. | 5.1 | 4.0 | 4.4 | 3.6 |
| Scattered Laser Energy Into DVDR (J) | 6.5 | 7.6 | 5.9 | 6.9 | 4.8 |
| Target Absorbed Energy (J) | 15.3 | 12.0 | 9.8 | 9.9 | 9.3 |
| Target X-ray Energy (J) | 0.4 | 0.6 | 0.5 | 0.5 | 0.3 |
| Charge Collector Symmetry (Ion Mass Collected by 4A/ Ion Mass Collected by 4B) | 0.84 | 0.76 | 0.83 | 0.74 | 0.93 |
| Laser Fluorescence on Target (mJ) | 1.3 | 2.0 | 1.6 | 2.3 | 2.4 |

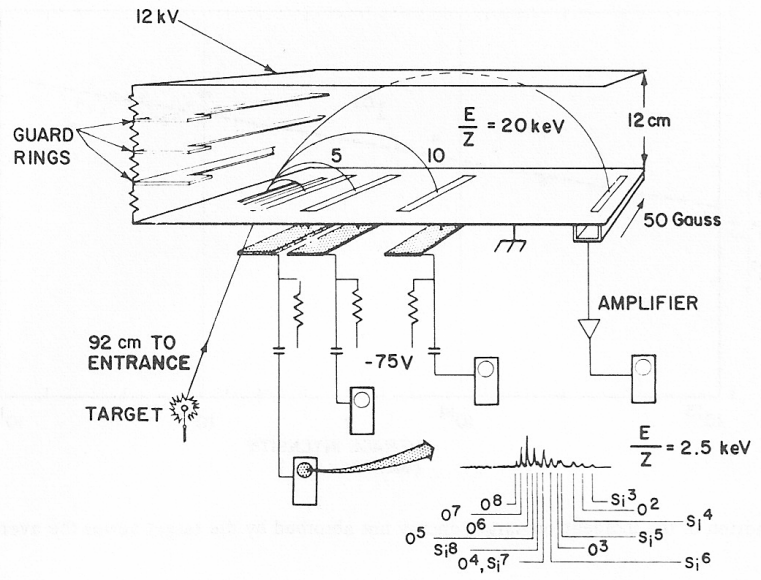


FIG.10. The mass spectrometer and a typical spectrum.

The mass spectrometer, shown in Fig.10, measures ion species and energy in the blowoff plasma. Ions entering at 45° to a static 1 kV/cm electric field follow parabolic trajectories characterized by the ion energy per unit charge (E/Z) and impinge on several Faraday ion detectors. The output of each ion detector is a time-of-flight sequence of A/Z pulses, where Z is the ion charge state. By this method, several points on the E/Z distribution of each A/Z species can be determined per shot [12, 13]. A typical ion spectrum from a DT-filled glass shell is also shown in Fig.10. Pulses characteristic of $O^{8+}$ through $O^{2+}$ and $Si^{8+}$ through $Si^{3+}$ are observed in the complex spectrum.

Charge-collector data obtained at 18 cm and 120 cm from the target show that little recombination or charge exchange occurs over 18 to 120 cm. The spectrometer with its entrance aperture at 92 cm from the target can therefore obtain an $\langle A/Z \rangle$ relevant to the charge collectors at 18 cm. Data from the target shots of Table I provide an estimate of $\langle A/Z \rangle \cong 4$.

Target experiments in a background gas of 20 torr helium have also been performed. The time history of the self-luminous blast-wave expansion is recorded with the Imacon 600 streak camera. The pressure pulse from the shock is recorded with two piezoelectric pressure probes (Fig.4) in the DVDR. The target kinetic energy as determined from the blast wave dynamics is in good agreement with the charge-collector kinetic energy measurements when the long range of the "fast"-ion-energy deposition in the helium gas is taken into account [14].

An ultrafast shadowgraph/schlieren camera has been developed that utilizes a 30-ps pulse from the main oscillator. The 30-ps pulse is amplified, frequency-doubled, delayed in time and used to back-illuminate the laser targets in a direction perpendicular to the main-beam optical axis. (Fig.4) The pictures so obtained are used to monitor target-disassembly symmetry and blast-wave formation in helium gas.

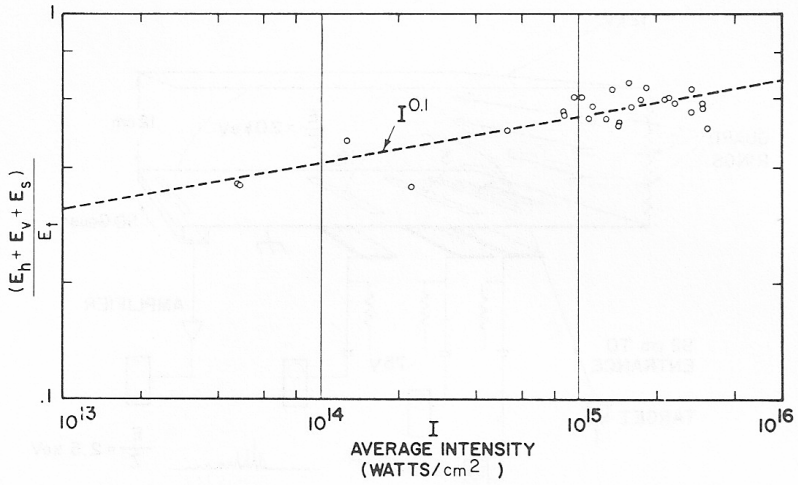


FIG.11. Fraction of the incident on-target energy not absorbed by the target versus the average intensity.

## 5.4. Energy balance

The laser energy refracted and scattered ($E_s$) at 90° to the optical axis measured with a calorimeter in the DVDR. This energy plus the vertically ($E_v$) and horizontally ($E_h$) polarized reflected energy is the total measured non-absorbed laser energy. In Fig.11, this non-absorbed energy, normalized to the incident energy ($E_t$).is plotted versus the average intensity on the target. The average intensity is calculated from the measured energy on target, the illuminated area of the target, and the width of the laser pulse (FWHM) as measured with the ultrafast photodiode. The on-target energy minus the non-absorbed energy is an upper bound on the sum of target kinetic energy and X-ray energy.

The X-ray energy as measured by the TLDs plus the kinetic energy as measured by the charge collectors represents the amount of laser energy coupled to the target. A second independent measurement of the target kinetic energy plus X-ray energy is made by a matched pair of differential calorimeters[3] located in the DVDR (Fig.4). One calorimeter is covered by a 1.06 $\mu$m bandpass filter and measures the 1.06 $\mu$m laser energy scattered by the target at 90° to the optical axis. The other calorimeter is uncovered and measures the scattered laser light as well as the X-ray energy and the target kinetic energy. The difference between the two calorimeter measurements is the particle energy plus X-ray energy. The differential-calorimeter measurement is then compared with the charge-collector-plus-TLD measurements. The agreement is usually better than 20%.

Energy balance is determined on each laser shot by summing the individual energy partitions: 1) horizontally polarized reflected 1.06 $\mu$m energy, 2) vertically polarized reflected 1.06 $\mu$m energy, 3) 1.06 $\mu$m energy scattered out between the ellipsoidal mirrors, 4) target kinetic energy and 5) X-ray energy. A comparison of this sum with the energy on target gives agreement to within about 15%. For example, on the average, for the shots in Table I,

[3] Gen-Tec.Ins., Model ED-200 Joulemeter, Quebec, Canada.

45% of the energy was reflected horizontally polarized, 8.8% was reflected vertically polarized, 9.6% of the energy was scattered out between the ellipsoidal mirrors, and 23% of the laser energy appeared as particle kinetic energy plus X-ray energy.

## 5.5. Target compression measurements

Target compression measurements are made with two X-ray pinhole cameras located in the DVDR (Fig.4). Both camera pinholes are 3 cm from the target. The upper and lower cameras have magnifications of 4 and 15 respectively. A typical camera resolution at the target is 14 $\mu$m for a 10 $\mu$m diameter pinhole and magnification of 4. The upper camera (5A) records the magnified target X-ray image filtered through 17.5 $\mu$m of aluminium on Kodak No-Screen X-ray film. Diametric scans of the pinhole photographic image are made with a microdensitometer. The film-density record, pinhole optics, and the film sensitivity are then used to determine the time-integrated spatial distribution of the X-ray emission. The lower camera (5B) records the magnified target X-ray image filtered through 50 $\mu$m of beryllium and intensified ($\times 10^6$) by a Chevron electron-multiplier array[4]. The image is photographed by a conventional 35 mm single-lens reflex camera.

Two basic mechanisms produce strong X-ray emission from the glass shell targets. First, the hot dense region heated by electron thermal conduction during the laser pulse radiates at the shell edge. If the shell is weakly accelerated, the X-ray emitting region remains at approximately the initial shell radius. Experimentally, this occurs when the on-target energy is less than about 0.7 J per nanogram of target mass. An example is shown in Fig. 12a.

The second mechanism for strong X-ray emission occurs when the imploding shell is turned around by the back pressure of the highly compressed and heated DT-gas. When the inward-directed energy of the shell is converted to thermal energy at the turn-around, the shell again radiates strongly. Hence, an X-ray pinhole image consisting of two concentric rings is expected. Such an image is shown in Fig. 12b. The observed volume compression, determined from the diameter of the inner ring, is about 125.

The X-ray emission due to each of the two mechanisms will be radially smeared by movement of the shell wall. A rapidly accelerated shell will therefore show a broadened outer ring in the X-ray pinhole image. Also, greater kinetic energy in the inward motion of the shell will lead to a smaller turn-around radius and an inner ring which is smeared toward the centre. If the turn-around radius is less than the resolution limit of the pinhole camera, the inner ring will fill in to a smooth central peak, such as that shown in Fig. 12c. Pinhole photographs similar to Fig. 12c are characteristic of target experiments having the highest neutron yields. In these high-yield experiments, the on-target energy exceeds 0.7 J per nanogram of target mass.

---

[4] Galileo Electro Optics Inc., Sturbridge, Mass., USA.

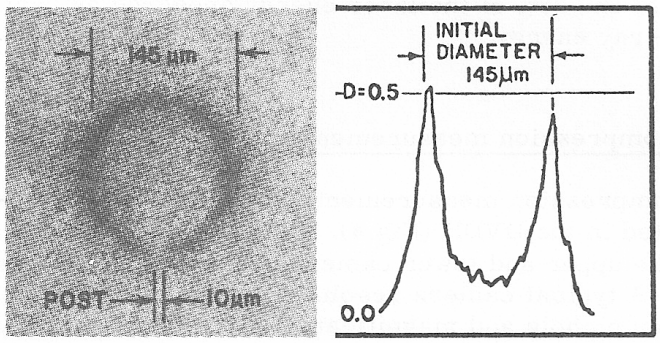


(a)

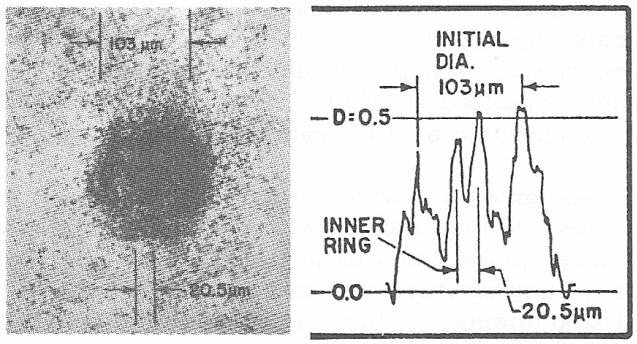


(b)

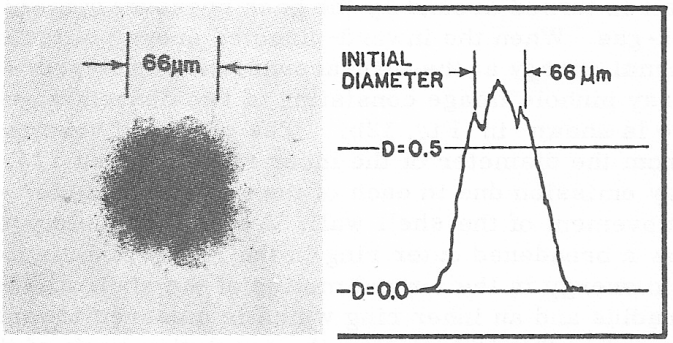


(c)

FIG. 12. X-ray pinhole photographs:
a) Energy on target per unit mass (0.2 J/ng);
b) Energy on target per unit mass (1.0 J/ng);
c) Energy on target per unit mass (1.5 J/ng), neutron event 1 in Table I.

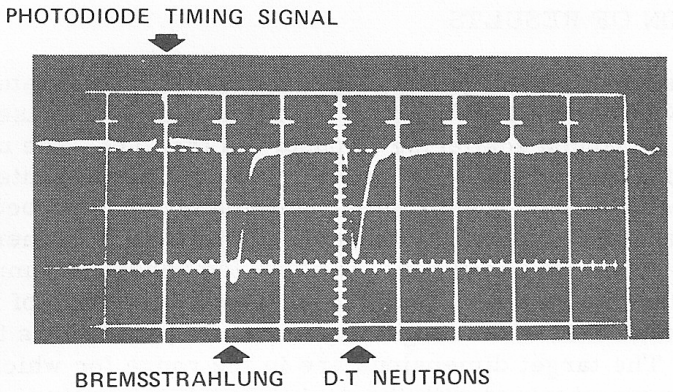


FIG.13. Neutron detector oscilloscope trace (NE-102-SPM).

## 5.6. Neutron measurements

Neutron-yield and time-of-flight measurements are provided by four scintillator-photomultiplier detectors (SMPs); two NE-104 scintillators (5.1 cm dia. × 2.5 cm thick) and two NE-102 scintillators (one 12.7 cm dia. × 5.1 cm thick and one 17.8 cm dia. × 10.2 cm thick).

The NE-104[5] SPMs have a time resolution of 2 ns and the NE-102 SPMs have a time resolution of 6 ns. These SPMs are located outside the target chamber (Fig.5). Neutron time-of-flight to the SPM is determined with reference to a photodiode timing mark (Fig.13) which indicates the arrival of the laser energy on target. A standard silver counter [15] is used to measure total neutron yields above $10^6$.

A typical neutron event detected by the 17.8 cm dia. NE-102 SPM at a distance of 6.64 m is shown in Fig. 13. The neutron signal follows the bremsstrahlung signal by 106 ns which is the correct time-of-flight difference for the 14.1-MeV neutrons from the DT reaction. The neutron signal in Fig. 13 represents the output from six neutrons arriving simultaneously.

Some of the target shots with higher neutron yields are shown in Table I. Within the time resolution limit of the SPMs, the measured neutron flight times from the target to the SPMs agree with the calculated time of flight for 14.1-MeV neutrons. This is strong evidence that the neutrons were created at the target and not at some secondary source position in the vacuum chamber [16].

---

[5] Nuclear Enterprise Inc., San Carlos, Calif., USA.

## 6. DISCUSSION OF RESULTS

In these experiments, spherical glass shells are irradiated with intensities from $4 \times 10^{13}$ to $4 \times 10^{15}$ W/cm$^2$. Over this range, no onset of anomalous absorption or enhanced scattering is observed (Fig.11). The non-absorbed laser energy follows a slow ($\sim I^{0.1}$) power law scaling with intensity. Although the "fast" ions represent a substantial fraction of the absorbed laser energy, this fraction shows only a slight tendency to increase at higher intensities, again with no threshold behaviour. The low-temperature component of the X-ray spectrum remains less than 1.3 keV over this range of intensities.

Table I summarizes the target experimental parameters for selected target shots. The target dimensions are in the range for which the largest neutron yields are obtained with the designated laser pulses. All of these target shots generate an X-ray pinhole photograph similar to that of Fig.12c.

The charge collector symmetry shown in Table I is indicative of the target disassembly symmetry required for neutron yields above $10^5$. Degraded compression symmetry and reduced neutron yield are observed whenever asymmetry of the laser-target illumination is intentionally introduced. For example, one-sided illumination of the target results in crescent shaped pinhole photographs with no central compression peak and no observable neutron yield. Also, delaying the laser energy in one channel 40 to 120 ps with respect to the other results in off-centre, degraded compressions and substantially reduced neutron yields.

X-ray pinhole photographs from experiments on neon-DT-filled shells[6] (17% neon by pressure) showed a factor-of-4 enhancement in the radiation from the central peak over that obtained in experiments on otherwise identical DT-filled shells. These photographs provide a direct observation of compression and hydrodynamic heating of the neon gas. Assuming that the neon contamination does not affect the compression hydrodynamics, these experiments indicate that the amount of shell material mixing with the DT-gas is less than the amount of neon contaminant.

The core temperature obtained in the target compression can be estimated with a simple model of the shell-driven gas-compression-expansion cycle [17]. The neutron yield obtained using this model is given by,

$$N_{DT} = 3 \times 10^{-28} n_i^2 R_i^4 C^{2/3} \theta_0^6$$

where $n_i$ is the initial deuterium or tritium particle density, $R_i$ is the initial sphere radius (cm), C is the volume compression and $\theta_0$ is the core temperature (keV) at peak compression. Taking $R_i = 35$ $\mu$m, $n_i = 1.5 \times 10^{21}$ atoms/cm$^3$, a compression (pinhole resolution limited) of C = 100, and setting $N_{DT} = 3 \times 10^5$, the core temperature is calculated to be $\theta_0 = 700$ eV. A higher compression implies a lower temperature; if C = 1000, then $\theta_0 = 540$ eV. The target shot corresponding to the pinhole photograph of Fig. 12b produced less than the detection-threshold neutron yield of $\sim 5 \times 10^3$. For this target $R_i = 51.5$ $\mu$m and C = 125, giving a central temperature less than 240 eV.

---

[6] These experiments were first suggested by P. Hammerling of the KMS Fusion theoretical group.

The present neutron yield level is not sufficient to experimentally observe the ion thermal broadening of the 14.1-MeV neutron line [18]. A DT neutron yield of $10^7$ - $10^8$ and a peak temperature of ~ 4 keV should allow a direct measurement of the compressed core temperature.

## 7. CONCLUSIONS

The experiments described above have directly observed laser heating, target compression, and hydrodynamic heating. The observed neutron production is correlated with compressed targets and is consistent with core temperatures of 0.5 to 0.7 MeV. These results sobstantially confirm some of the basic concepts of laser-driven fusion and provide strong encouragement to extend the experiments to higher laser energies and a larger class of fusion targets.

## ACKNOWLEDGEMENTS

The authors gratefully acknowledge the inspiration and leadership of Dr. Keith A. Brueckner, whose theoretical insights led to the inception of the KMS Fusion programme and guided its development. We wish also to acknowledge with gratitude the direction of and participation in the laboratory programme by Dr. Robert Hofstadter, which contributed in large measure to the success of the experiments reported in this paper.

The authors also acknowledge the valuable assistance of W. Lawrence, R. Sanderson, and J. Vidolich in operating the laser system, and of E. Benn, D. Burgeson, C. Cheng, P. Fairchild, R. Nolen, R. Sigler and D. Sullivan in the laser-target experiments.

## REFERENCES

[1] BRUECKNER, K.A., Rev.Mod.Phys. 46 (1974) 325.
[2] NUCKOLLS, J., WOOD, L., THIESSEN, A., ZIMMERMAN, Nature (London) 239 (1972) 139.
[3] BASOV, N.G., BOIKO, V.A., ZAKHOROV, S.M., KROKHIN, D.N., SKLIZKOV, G.V., JETP Lett. 18 (1973) 184.
[4] SOURES, J., GOLDMAN, L.M., LUBIN, M., Nucl.Fusion 13 (1973) 829.
[5] SALERES, A., FLOUX, F., COGNARD, D., BOBIN, J.L., Phys.Lett. 45A (1973) 451.
[6] YAMANAKA, C., YAMANAKA, T., SASAKI, T., YOSHIDA, K., WAKI, M., KANG, H.B., Phys. Rev. A6 (1972) 2335.
[7] THOMAS, C.E., KMSF Report No. U-190, submitted to Appl.Opt.
[8] DOWNWARD, J.G., Bull.Am.Phys.Soc. 19 (1974) 886.
[9] MAYER, F.J., MONTRY, G.R., BENN, E., 23rd Annual Conf. for Appl. of X-ray Analysis, August 7-9, 1974, Denver, Colorado, KMSF Report No. U-187.
[10] JAHODA, F.C., LITTLE, E.M., QUINN, W.E., SAWYER, G.A., STRATTON, T.F., Phys.Rev. 119 (1960) 843.
[11] KUNZE, H.J., GABRIEL, A.H., GRIEM, H.R., Phys.Fluids 11 (1968) 662.
[12] ALLEN, F.J., Rev.Scient.Instrum. 10 (1971) 1423.
[13] GOFORTH, R.R., Bull.Am.Phys.Soc. 19 (1974) 909.
[14] MAYER, F.J., LEONARD, T.A., Bull.Am.Phys.Soc. 19 (1974) 914.
[15] LANTER, R.J., BANNERMAN, D.E., LASL Report No.LA-3498-MS, July 16, 1966.
[16] McCALL, G.H., YOUNG, F., EHLER, A.W., KEPHART, J.F., GODWIN, R.P., Phys.Rev.Lett. 30 (1973) 1116.
[17] OSBORN, R.K., MAYER, F.J., KMSF Report No. U-206.
[18] LEHNER, G., POHL, F., Z.Phys. 207 (1969) 83.

# DISCUSSION

## ON PAPER IAEA-CN-33/F 1

A.Y. WONG: There seems to be some asymmetry around the support of the pellet. Would you expect improvement in your compression ratio when and if the support could be removed?

R. JOHNSON: Experiments have been performed with 3-$\mu$m and 10-$\mu$m fibres. The pinhole photographs showed a shadow effect with the 10-$\mu$m fibre but this was not apparent when 3-$\mu$m fibres were used. Other experiments with 3-$\mu$m and 10-$\mu$m fibres did not indicate significant differences in neutron production.

A.Y. WONG: Do you observe hot ions moving towards the inner core? If so can such hot ions produce neutrons?

R. JOHNSON: The production of fast ions is not well understood at this time, but the number of inward-directed fast ions would be too small to account for the neutron production. Experiments with one-sided illumination show the presence of fast ions, while no compression or neutron production is observed.

H.A.B. BODIN: Can you say how the electron temperature varied with laser power – or power into the pellet?

R. JOHNSON: The important parameter is the temperature in the core and neutron production is a sensitive function of this. Neutron production in these experiments scales exponentially with intensity and the exponent factor is dependent on the size of the target.

E.B. GOLDMAN: Does the appearance of fast ions correlate with any other diagnostic such as hard X-rays?

R. JOHNSON: The fast ions are correlated to a hard component in the X-ray spectrum. The experiments which produce only few fast ions also have a spectrum which is close to Maxwellian.

E.B. GOLDMAN: Do you see fast ions on all shots?

R. JOHNSON: Fast ions are present on all neutron-producing target shots. Fast ions are not observed when we have a prepulse or high fluorescence levels.